Geophysical Research Letters

RESEARCH LETTER

10.1029/2022GL099798

Key Points:

- · Tonga volcano eruption during a magnetic storm recovery-phase triggered extreme equatorial plasma bubbles appearing even beyond Tokyo
- The volcano-induced wave perturbations and unusually strong pre-reversal enhancement (PRE) result in the rare development of plasma bubbles
- Reduced E-region conductivity by the wave propagation and enhanced F-region wind by negative storm at the equatorial anomaly intensify PRE

Supporting Information:

Supporting Information may be found in the online version of this article.

Correspondence to:

C. C. H. Lin, charles@mail.ncku.edu.tw

Citation:

Rajesh, P. K., Lin, C. C. H., Lin, J. T., Lin, C. Y., Liu, J. Y., Matsuo, T., et al. (2022). Extreme poleward expanding super plasma bubbles over Asia-Pacific region triggered by Tonga volcano eruption during the recovery-phase of geomagnetic storm. Geophysical Research Letters, 49, e2022GL099798. https://doi.org/10.1029/2022GL099798

Received 31 MAY 2022 Accepted 31 JUL 2022

Extreme Poleward Expanding Super Plasma Bubbles Over Asia-Pacific Region Triggered by Tonga Volcano Eruption **During the Recovery-Phase of Geomagnetic Storm**

P. K. Rajesh¹, C. C. H. Lin¹, J. T. Lin¹, C. Y. Lin^{2,3}, J. Y. Liu^{2,3}, T. Matsuo⁴ C. Y. Huang⁵, M. Y. Chou^{6,7}, J. Yue^{6,7}, M. Nishioka⁸, H. Jin⁸, J. M. Choi¹, S. P. Chen¹, Marty Chou¹, and H. F. Tsai¹

Department of Earth Sciences, National Cheng Kung University, Tainan, Taiwan, ²Center for Astronautical Physics and Engineering, National Central University, Taoyuan, Taiwan, 3Department of Space Science and Engineering, National Central University, Taoyuan, Taiwan, ⁴Ann and HJ Smead Department of Aerospace Engineering Sciences, University of Colorado, Boulder, CO, USA, 5National Space Organization, Hsinchu, Taiwan, 6NASA Goddard Space Flight Center, Community Coordinated Modeling Center, Greenbelt, MD, USA, ⁷Physics Department, Catholic University of America, Washington, DC, USA, 8The National Institute of Information and Communications Technology, Tokyo, Japan

Abstract The Tonga volcano eruption of 15 January 2022 unleashed a variety of atmospheric perturbations, coinciding with the recovery-phase of a geomagnetic storm. The ensuing thermospheric variations created rare display of extreme poleward-expanding conjugate plasma bubbles seen in the rate of total electron content index over 100-150°E, reaching ~40°N geographic latitude. This is associated with fluctuations in FORMOSAT-7/COSMIC-2 (F7/C2) ion-density measurements and spread-F in ionograms. Preceding to this, an unusually strong pre-reversal enhancement (PRE) occurred in the global ionospheric specification (GIS) electron density profiles derived from F7/C2 observations. The GIS also revealed a decrease of equatorial ionization anomaly (EIA) crest density due to the storm impact. Reduced E-region conductivity by volcano-induced waves and enhanced F-region wind, further accelerated by reduced ion-drag over the EIA, apparently intensified the PRE. Accompanied with the strong PRE, volcano-induced seed perturbations triggered the super plasma bubble activity.

Plain Language Summary Rare things could happen when the centennial volcanic eruption occurred at the late stages of a magnetic storm driven by solar wind disturbances. The volcanic eruption drove atmosphere waves at the lower altitude in the ionosphere and the storm effect enhanced eastward wind at higher altitudes. The combined effect led to an unusual and substantial uplift of the post-sunset ionosphere, known as pre-reversal enhancement (PRE). The large layer uplift destabilized the bottomside ionosphere, leading to vigorous bubble-like plasma irregularities, or plasma bubbles extending to middle latitudes, which are very rarely seen in January when the solar activity is low. This is the first time such super plasma bubbles are produced by the joint influence of geomagnetic and atmospheric forcings from above and below.

1. Introduction

Equatorial plasma bubbles (EPBs) are the irregularities in the post-sunset equatorial/low-latitude ionosphere, manifesting as spread-F in ionograms (Bekner & Wells, 1934), scintillations in radio signals (Whitney & Malik, 1968), bite-outs in ion-density measurements (Hanson & Sanatani, 1973), plume structures in radar maps (Woodman & La Hoz, 1976), and intensity depletions in airglow images (Weber et al., 1978). EPBs are initiated by Rayleigh-Taylor instability (Dungey, 1956) operating in the post-sunset bottom-side F-region where vertical plasma density gradient is anti-parallel to gravity, under favorable conditions of seed perturbations, sharper plasma density gradients, smaller ion-neutral collisions, and stronger vertical plasma drifts (Sultan, 1996). Several review articles discuss the history and progress in the theoretical and technical evolution of EPB monitoring (Farley et al., 1970; Glover, 1960; Hysell, 2000; Ossakow, 1981; Yokoyama, 2017).

Notwithstanding the numerous studies since the first known report, generation and occurrence of EPBs still remain as most intriguing ionospheric research topic. This continuing interest stems from the unpredictable occurrence of bubbles owing to various factors that control and contribute to their generation. The uncertainty arises from the variations of seed perturbation (Abdu et al., 2009; Kelley et al., 1981; Wu et al., 2015), neutral wind

© 2022. American Geophysical Union. All Rights Reserved.

RAJESH ET AL. 1 of 10

19448007, 2022, 15, Downloaded from https://agupubs.onlinelibrary.

wiley.com/doi/10.1029/2022GL099798, Wiley Online Library on [28/02/2023]. See the Terms and Conditions.

One of such major external factors controlling the occurrence of EPBs is geomagnetic storm (hereafter, storm), either amplifying or suppressing the bubble generation (Rajesh, Lin, Chen, Chen, et al., 2017; Rastogi et al., 1981; Whalen, 2002; R. W. Wright et al., 1956). The impact of prompt penetration and/or disturbance dynamo electric field, either aids or suppresses the pre-reversal enhancement (PRE), leading to the generation/inhibition of bubbles, and occasionally in the post-midnight irregularities (Aarons, 1991; Rajesh, Lin, Chen, Lin, et al., 2017; Sripathi et al., 2018). Occasionally, strong prompt penetration electric fields generate super plasma bubbles, reaching much higher latitudes (Aa et al., 2018; Cherniak & Zakharenkova, 2016; Ma & Maruyama, 2006). A unique case of the external influence on EPB generation was the recent eruption of the Tonga volcano (hereafter, the eruption) on 15 January 2022, triggering significant EPB activity (Aa et al., 2022; Sun et al., 2022).

The eruption caused unprecedented perturbations in the atmosphere and ionosphere (C. Wright et al., 2022; J. T. Lin et al., 2022; Themens et al., 2022), for the first-time showing ionosphere variations in conjugate hemispheres far away from the source much earlier than anticipated (J. T. Lin et al., 2022). Such disturbed conditions are explained to have triggered the EPBs across wide longitudes (Aa et al., 2022). This study reports very intense and rare super plasma bubbles over the Asia-Pacific region (100–160°) compared to other longitudes, reaching magnetic latitudes (MagLat) of ~35°. Such super plasma bubbles triggered by a volcano eruption are unheard of, and the reasoning based on eruption-induced perturbations (Aa et al., 2022; Sun et al., 2022) could not explain these extreme EPBs specific to this region. The eruption occurred in the recovery-phase of a moderate storm (for the storm description, see J. T. Lin et al., 2022), a rare coincidence of two such events. This paper discusses the plausible mechanisms that pre-condition the ionosphere and generate the super plasma bubbles over the Asia-Pacific by the combined effects of the eruption and storm-induced variations.

2. Data Analysis

This study uses the total electron content (TEC) measurements from ground-based global navigation satellite system (GNSS) receivers, ionograms over Japan and Australia, in-situ and radio occultation (RO) measurements by FORMOSAT-7/COSMIC-2 (F7/C2) satellites, and the Global Ionospheric Specification (GIS) electron density profiles constructed by assimilating F7/C2 RO and GNSS slant TECs (C. Y. Lin et al., 2017). The GNSS networks in New Zealand, Australia, Japan and Taiwan are used to derive vertical TEC, and the occurrence and evolution of EPBs by calculating the rate of TEC index (ROTI) with an averaging period of 5-min (Pi et al., 1997). To distinguish the ROTI by volcanogenic TIDs, the TEC variations are also examined by applying a 10–60-min bandpass filter (e.g., J. T. Lin et al., 2022).

The ionosonde stations at Kokubunji (Japan) and Townsville (Australia) allow the examination of the onset and development of spread-F at either side of the magnetic equator. In-situ ion density measurements by F7/C2 ion velocity meter (IVM) detect plasma irregularities along satellite track. The GIS has been validated with ionosonde measurements (C. -Y. Lin et al., 2020), and applied to study day-to-day ionosphere variability (Rajesh, Lin, Lin, et al., 2021), ionospheric response to geomagnetic storms (Rajesh, Lin, Lin, Chen, et al., 2021), and sudden stratospheric warmings (J. T. Lin et al., 2019, 2020). Here, the average of three previous quiet-days (11–13 January) GIS is used as reference to quantify the variations.

3. Results

Figure 1 displays the absolute TEC, ROTI, and filtered TEC over the Asia-Pacific longitudes at the selected time intervals of ~0941 and ~1123 UT, following the eruption. A stripe of very low TEC, marked by red arrow, is seen above Australia over ~145°E and 10–20°S, though no such pattern exists over Japan possibly due to the low background. While such a depletion resembling EPB is rare to be spotted in background TEC, the most striking features are the strong ROTI coinciding with the depletion, confirming intense plasma irregularities over this region. These ROTI enhancements show remarkable conjugate pattern, appearing over both Australia and Japan, exhibiting reverse C-shape. The filtered TEC maps in Figure 1 show concentric TIDs generated by the volcano-induced Lamb-waves. Based on the locations and orientation, the strong ROTI regions are apparently

RAJESH ET AL. 2 of 10

19448007, 2022, 15, Downloaded from https://agupubs.onlinelibrary.wiley.com/doi/10.1029/2022GL099798, Wiley Online Library on [28/02/2023]. See the Terms and Conditions (https://online

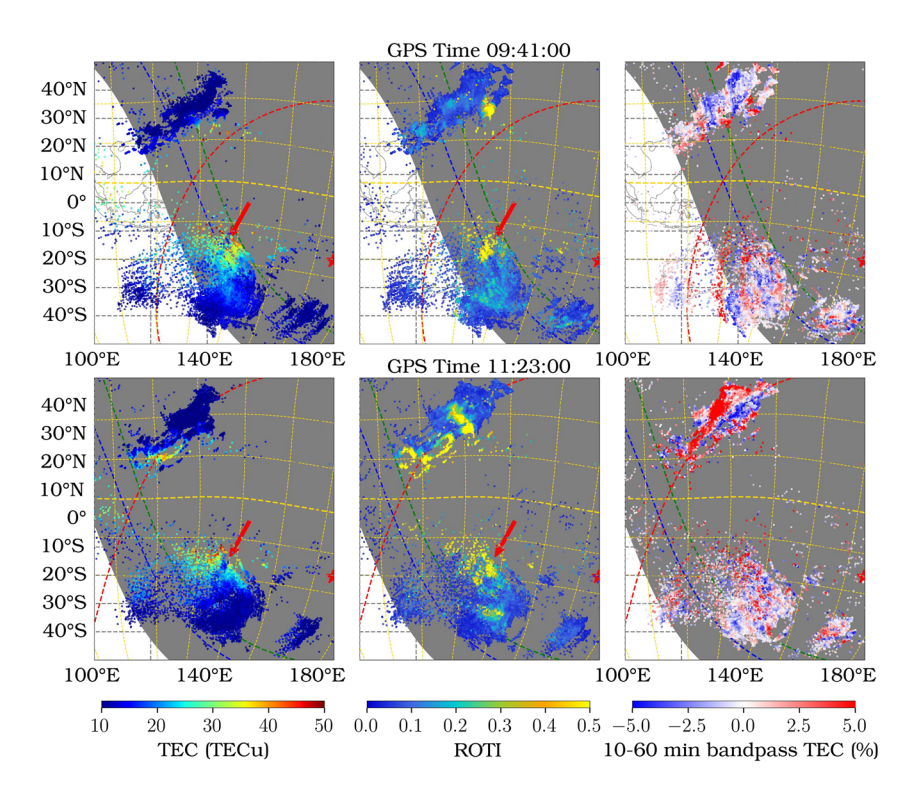


Figure 1. Ionospheric disturbances after the eruption in (left) absolute total electron content (TEC), (middle) rate of TEC index (ROTI), and (right) 10–60-min band-pass filtered TEC at (top) 0941 and (bottom) 1123 UT, respectively. The red arrow in the left panels indicate TEC depletions, and co-located strong ROTI. The red-dashed lines show the Lamb-wave (see J. T. Lin et al., 2022). The gray-shaded regions are under sunset with the blue- and green-dashed lines representing the E- and F-region terminators. The yellow grids give geomagnetic coordinates with thick dashed-line denoting magnetic equator.

unrelated to these TIDs. Though plasma irregularities occurred across several longitudes on this night (Aa et al., 2022), extreme and intense irregularities appeared only over the Asia-Pacific region (Figure S1 in Supporting Information S1), which is investigated here.

Figure 2 details the time evolution of enhanced ROTI, portraying the poleward expanding irregularities in succession in the western longitudes with the sunset. The poleward expanding ROTI regions over eastern longitudes of Japan and Australia at 0945 UT appear magnetically conjugate, with identical westward tilt at the poleward ends. This conjugate alignment is evident in the subsequent frames, also for the second strong ROTI region appearing to the west at 1030 UT. As time progresses, these ROTI regions expand further poleward with their locations slowly shifting eastward and, new irregularities developing to the west. The irregularities exhibit westward tilt typical of EPBs, reaching maximum poleward latitudes of ~35°N MagLat.

The F7/C2 IVM ion density in Figure 2 also shows perturbations when the satellites overpass the longitudes of strong ROTI under F-region sunset. At 0945 UT, the IVM scanning over 10–15° MagLat detected two consecutive plasma bubbles, where the eastern bubble aligns with the conjugate structure of the strong ROTI poleward to it, confirming that the ROTI values are related to vertically rising EPBs. The second bubble to its west is also aligned with the strong ROTI that was about to emerge over Japan region, indicating EPBs are still evolving. At 1000 UT, a second F7/C2 IVM also scans the same EPBs, with latter passing over latitudes just to the south of the magnetic equator, ascertaining that the strong ROTI regions are linked to the EPBs. This further offers a rare opportunity to gain multi-point perspectives of the same plasma bubbles at equatorial, low- and mid-latitude locations by combining ground-based and in-situ platforms. At 1130 UT, two such IVM scans over 120°E show irregularities near the equator and over the strong ROTI regions at low-latitudes, once again providing evidence that the strong ROTI are associated with field-aligned EPBs.

A movie of these observations featuring the time-evolution of the irregularities is provided as Supporting Information (Movie \$1), which also includes the corresponding absolute and filtered TECs. Though the concentric TIDs

RAJESH ET AL. 3 of 10

19448007, 2022, 15, Downloaded from https://agupubs.onlinelibrary.wiley.com/doi/10.1029/2022GL099798, Wiley Online Library on [28/02/2023]. See the Terms and Conditions (https://agupubs.onlinelibrary.wiley.com/doi/10.1029/2022GL099798, Wiley Online Library on [28/02/2023]. See the Terms and Conditions (https://agupubs.onlinelibrary.wiley.com/doi/10.1029/2022GL099798, Wiley Online Library on [28/02/2023]. See the Terms and Conditions (https://agupubs.onlinelibrary.wiley.com/doi/10.1029/2022GL099798, Wiley Online Library on [28/02/2023]. See the Terms and Conditions (https://agupubs.onlinelibrary.wiley.com/doi/10.1029/2022GL099798, Wiley Online Library on [28/02/2023]. See the Terms and Conditions (https://agupubs.onlinelibrary.wiley.com/doi/10.1029/2022GL099798, Wiley Online Library.wiley.com/doi/10.1029/2022GL099798, Wiley Online Library

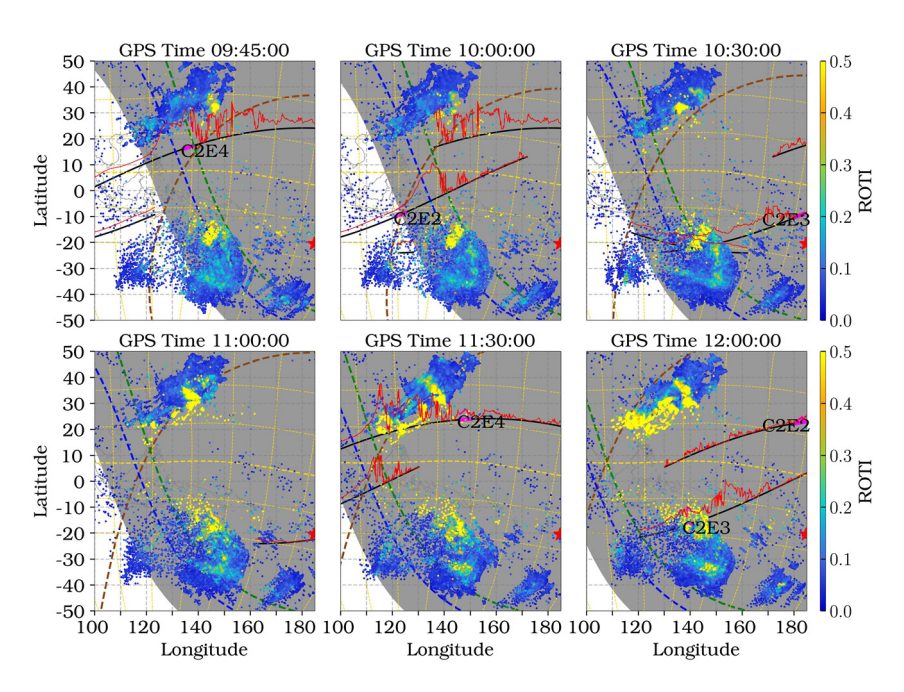


Figure 2. Similar to Figure 1, but only the rate of TEC index (ROTI) maps at selected intervals, illustrating the poleward development of Equatorial plasma bubbles. Also plotted are the overpasses of F7/C2 during ± 15 min (black lines), with the red lines showing ion velocity meter (IVM) ion density measurements. Brown dashed lines are used for the Lamb-wave locations

after the eruption yield strong ROTI, they essentially propagate westwards over Australia and north-westward over Japan (Movie S1). In contrast, the poleward expanding ROTI bands appear mostly stationary, and show an eastward-moving tendency (Figure 2 and Movie S1), corroborating their EPB link.

The apex projection of ROTI in Figure 3 illustrates the extreme altitudes attained by the irregularities over the equator, offering a unique view resembling towering giant plume structures seen in JULIA radar measurements (Hysell & Burcham, 1998). The irregularities here penetrate as high as ~3000 km, whereas the maximum altitudes in radar maps are usually <1000 km, demonstrating the intense nature of the EPBs triggered after the eruption. The apex projection further facilitates the estimation of vertical rise velocities of the EPBs, revealing rapidly upward drifting irregularities at speeds of 420–280 m/s till altitudes of ~1500 km and drops below 200 m/s as the bubbles rise further (Figure S2 in Supporting Information S1). Such large upward velocities enable the irregularities to reach extreme poleward latitudes. Strong spread-F was recorded in the ionograms over Kokubunji (28.8°N MagLat; 139.5°E) and Townsville (28.4°S MagLat.; 146.8°E) on this evening (Figure S3 in Supporting Information S1), independently confirming the irregularities observed in ROTI maps at such large magnetic latitudes.

To understand the background electron density distribution, GIS maps at 300 km during 0730–1030 UT are stacked together in Figures 4e–4h, with the average of previous three quiet-days as reference (a–d), along with the difference between the two (i–l). The GIS include measurements taken within ±30 min of the marked times. Note a sharp collapse of the southern equatorial ionization anomaly (EIA) crest over the sunlit longitudes and strengthening of the northern crest at earlier local-time sectors compared to the reference. The crest separation is drastically reduced. The variations along the sunset terminator over the Asia-Pacific longitudes on the eruption day are even more dramatic, with the enhanced EIA crest latitudes surpassing the corresponding noon-time locations, indicating an extremely intense PRE, almost coinciding with the arrival of the Lamb-wave over the magnetic equator. Panels (e–h) demonstrates the collapse of the dayside EIA density structure, especially the southern crest, with an equatorward displacement of the crest latitude and the intense PRE in the evening sector.

The vertical slices at 140° E in Figures 4m–4p further show how intense the PRE was in this evening. At 0930 UT (~1850 LT) the F-peak altitude (hmF₂) is approximately 525 km (Figure 4n), which is ~200 km above the corresponding reference value (Figure 4m), with extremely low electron density underneath. About 1-hr later, the PRE further strengthened, with the hmF₂ over the magnetic equator rising above 550 km altitude (Figure 4p).

RAJESH ET AL. 4 of 10

1944807, 2022, 15, Dowloaded from https://agupubs.onlinelibrary.wity.co.or/doi/10.1029/2023GL099798, Wiley Online Library on [28/02/2023]. See the Terms and Conditions (https://onlinelibrary.witey.com/terms-and-conditions) on Wiley Online Library for rules of use; OA articles are governed by the applicable Creative and Conditions (https://onlinelibrary.witey.com/terms-and-conditions) on Wiley Online Library for rules of use; OA articles are governed by the applicable Creative and Conditions (https://onlinelibrary.witey.com/terms-and-conditions) on Wiley Online Library for rules of use; OA articles are governed by the applicable Creative and Conditions (https://onlinelibrary.witey.com/terms-and-conditions) on Wiley Online Library for rules of use; OA articles are governed by the applicable Creative and Conditions (https://onlinelibrary.witey.com/terms-and-conditions) on Wiley Online Library for rules of use; OA articles are governed by the applicable Creative and Conditions (https://onlinelibrary.witey.com/terms-and-conditions) on Wiley Online Library for rules of use; OA articles are governed by the applicable Creative and Conditions (https://onlinelibrary.witey.com/terms-and-conditions) on Wiley Online Library for rules of use; OA articles are governed by the applicable Creative and Conditions (https://onlinelibrary.witey.com/terms-and-conditions) on Wiley Online Library for rules of use; OA articles are governed by the applicable Creative and Conditions (https://onlinelibrary.witey.com/terms-and-conditions) on Wiley Online Library for rules of use; OA articles are governed by the applicable Creative and Conditions (https://onlinelibrary.witey.com/terms-and-conditions) on Wiley Online Library for rules of use; OA articles are governed by the applicable Creative and Conditions (https://onlinelibrary.witey.com/terms-and-conditions) on Wiley Online Library for rules of use; OA articles are governed by the applicable Creative and Conditions (https://onlinelibrary.witey.com/terms-and-conditions) on Wiley Online Lib

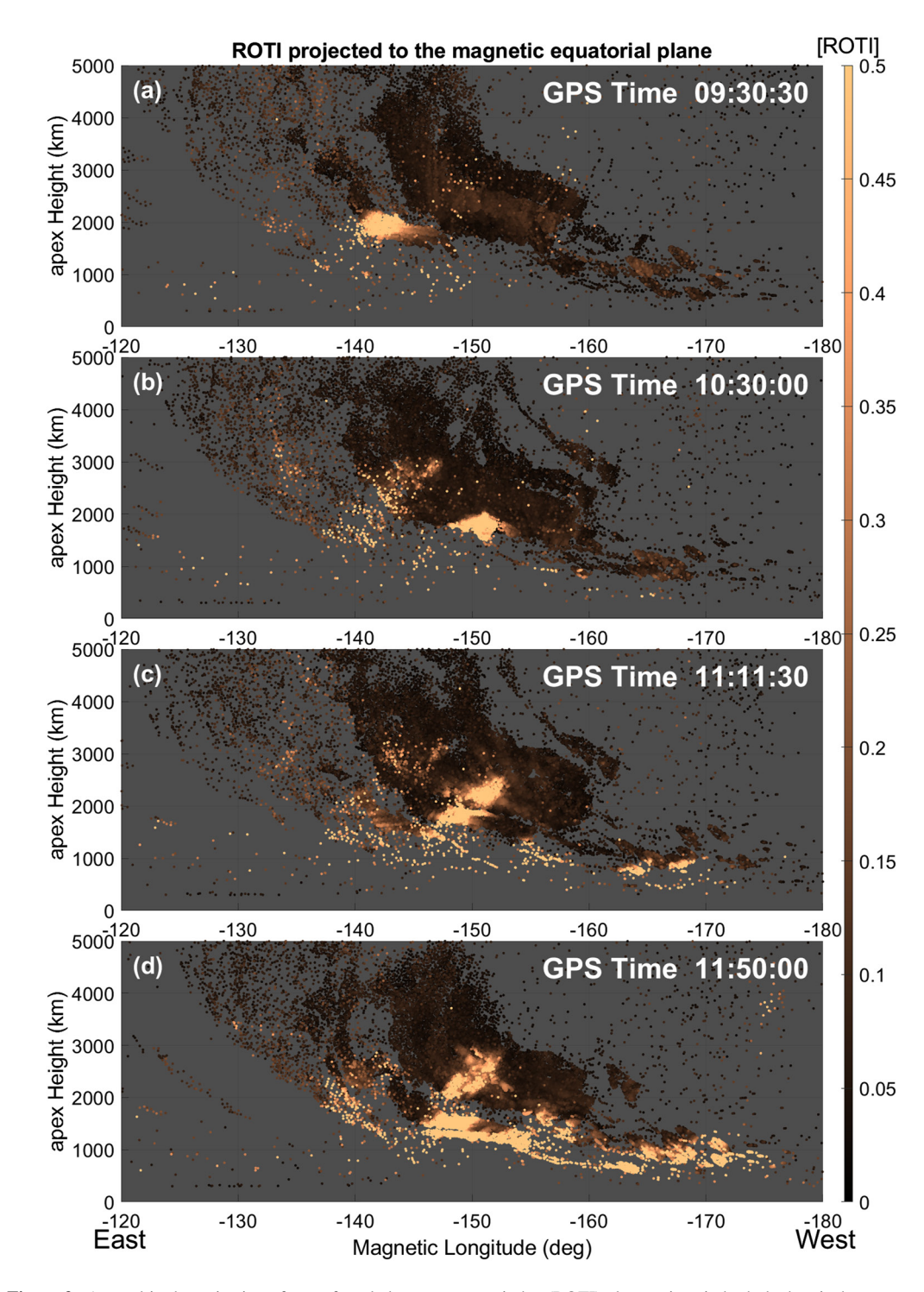


Figure 3. Apex altitude projection of rate of total electron content index (ROTI) observations in both the hemisphere at selected intervals after the eruption.

The overplotted vertical electron density gradient peaks over 350–450 km altitudes, much higher than the 220 km reference height. The vertical variation of hmF_2 estimated from GIS over 140°E during 0700–1000 UT yields ~40 m/s, three times the reference value (Figure S4 in Supporting Information S1).

RAJESH ET AL. 5 of 10

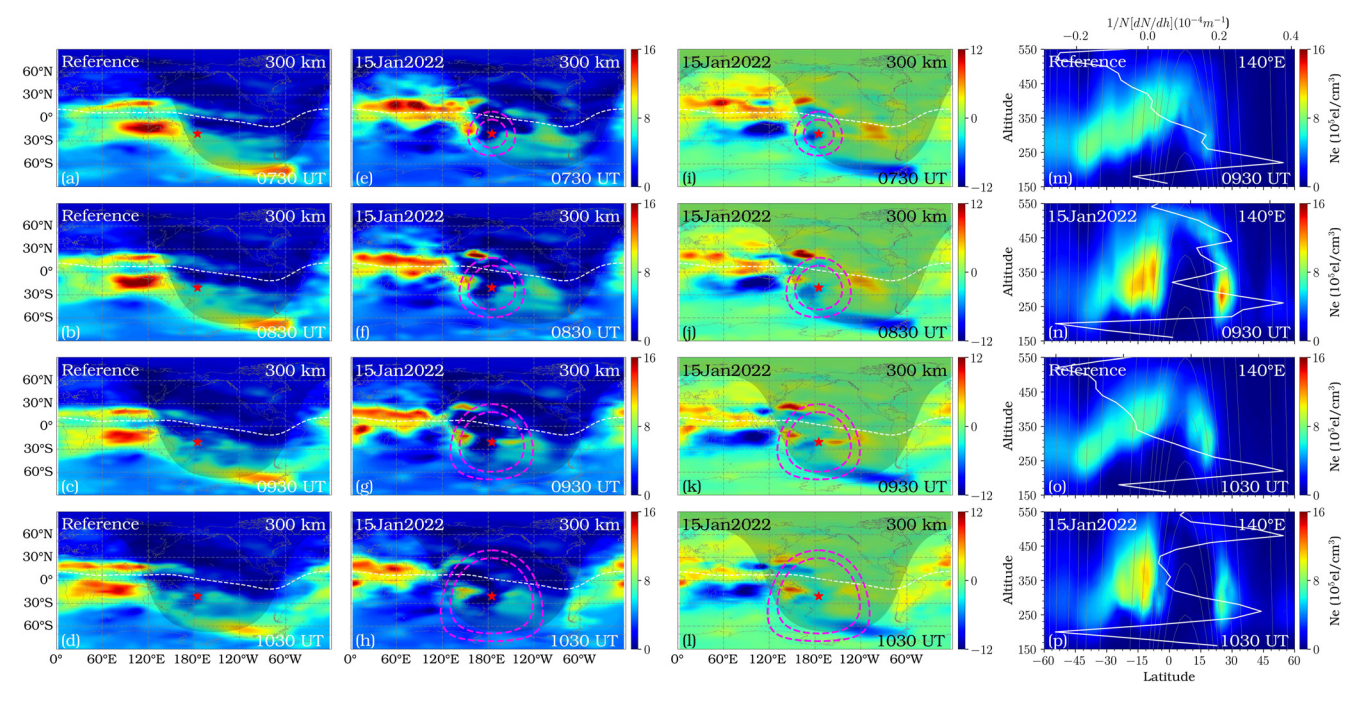


Figure 4. Global ionospheric specification (GIS) electron density maps. Panels (a–d) gives reference day plots, (e–h) on the eruption day, and (i–l) their differences at 300 km during 0730–1030 UT. The white dashed lines represent magnetic equator, and the red-dashed curves (second and third columns) are the Lamb-wave locations during the ± 30 min period of GIS assimilation. The red asterisk denotes the location of Tonga. The sunset longitudes are shaded. The latitude-altitude maps in panels (n and p) illustrate intense PRE on 15 January compared to reference day in (m and o). The white solid lines in (m–p) denote the altitude gradient of electron density.

4. Discussion

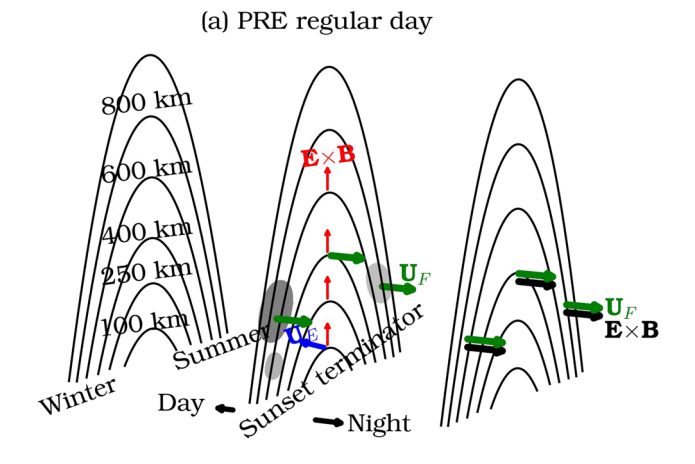
The phenomenal Tonga volcano eruption perturbed the post-sunset electron density distribution over the entire Asia-Pacific longitudes spanning several thousands of kilometers, producing EPBs that lasted several hours. The meridionally-extended bands of strong ROTI in the conjugate hemispheres after the eruption, with characteristic reverse C-shape often seen in airglow depletions, offer a unique perspective of the EPBs thus far reported by GNSS observations (Figures 1 and 2, Movie S1). Aa et al. (2022), and Sun et al. (2022) detailed the morphology of these EPBs, showing irregularities across East Asia to East Africa, reaching maximum altitudes of 1500–2000 km, though distinct, field-aligned, conjugate EPBs could not be distinguished, probably limited by their data coverage. The apex altitude projection here (Figure 3) uniquely illustrates the extreme nature of the irregularities, giving the perception of giant plume structures penetrating to even 3000 km. Such wide-spread, long-lasting, and extremely upward/poleward expanding super plasma bubbles after a volcano eruption are observed for the first time, revealing the space weather consequences triggered by seismic activities occurring far below the ground.

The prevailing solstice conditions over the Asia-Pacific longitudes in the middle of January, yielding stronger inter-hemispheric winds and inclined alignment of solar terminator with magnetic meridian least favors EPB generation (Burke et al., 2004; Nishioka et al., 2008). According to Aa et al. (2022) and Sun et al. (2022), strong perturbations following the eruption provided suitable conditions and initial seeding for the irregularities, ruling out any storm-induced influence. Although irregularities could still grow with such seed perturbations (McClure et al., 1998; Tsunoda, 2010b), the super plasma bubbles over the Asia-Pacific (Figure S1 in Supporting Information S1) remain unexplained. The discussion below examines the plausible mechanisms that could produce such rapidly expanding irregularities, including the factors for the post-sunset uplift of the F-layer, and the possible influence of the storm-induced variations.

The GIS observations (Figures 4 and S4 in Supporting Information S1) provide first-hand evidence for the extremely intense PRE that persisted for \sim 3-hr, lifting the F-layer \sim 200 km and producing sharp plasma density gradient at altitudes of \sim 500 km. The seed perturbations by the eruption could instigate EPBs at such elevated F-region bottom-side, which can subsequently rise to much higher altitudes. Nonetheless, such strong PRE of \sim 40 m/s (Figures 3 and S4 in Supporting Information S1) over these longitudes in solstice under low solar

RAJESH ET AL. 6 of 10

19448007, 2022, 15, Downloaded from https://agupubs.onlinelibrary.wiley.com/doi/10.1029/2022GL099798, Wiley Online Library on [28/02/2023]. See the Terms and Conditions (https://online



 \mathbf{U}_F : F-region zonal wind \mathbf{U}_E : E-region zonal wind

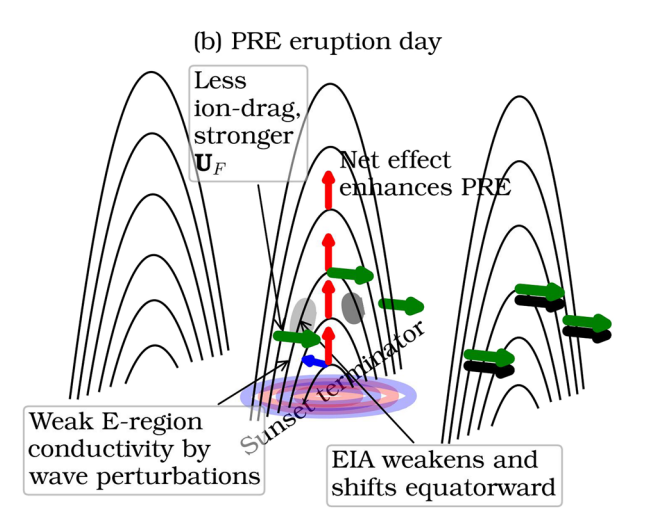


Figure 5. Sketch illustrating pre-reversal enhancement (PRE). (a) On a regular solstice day where finite E-region conductivity in winter hemisphere yields weak or no PRE. (b) After the eruption during storm recovery. $E \times B$ drift by gravity-waves (blue/red rings) decreases E-region conductivity, favoring PRE. Weakened equatorial ionization anomaly (EIA) (gray-shaded area) by storm and eruption enable stronger \mathbf{U}_F , mobilizing ions and yielding upward vortical flow over the equator to supply more plasma, strengthening the PRE.

activity is unusual. Also, E-region conductivity is crucial for the generation of PRE (Richmond, Fang, & Maute., 2015), where the finite conductivity in the winter hemisphere would inhibit the development of polarization electric fields by F-region dynamo. The wave perturbations by the eruption (e.g., J. T. Lin et al., 2022) could reduce the E-region Pederson conductivity through ExB drifts (Chou et al., 2021), supporting the development of PRE here. Sharp decrease of electron density is reported related to such seismic events (Shinagawa et al., 2013; Zettergren et al., 2017). The dynamo electric fields associated with the strong neutral wind perturbations after the eruption (Harding et al., 2022; Le et al., 2022) could further elevate the ionosphere through ExB drifts (Huba et al., 2015).

Moreover, the storm disturbance dynamo weakened the equatorial fountain (e.g., C. H. Lin et al., 2007) and yielded positive (negative) responses in the winter (summer) hemisphere in mid-latitude due to composition disturbances (Fuller-Rowell et al., 1996). Hence, the EIA crests on the eruption day move closer to the magnetic equator, producing sharp electron density decrease in the southern hemisphere (Figure 4). Near the terminator, the diminished EIA crest density would enable stronger F-region eastward wind due to reduced ion-drag. Richmond and Fang (2015) demonstrated that F-region zonal winds over EIA is crucial in controlling the PRE strength. The stronger wind would mobilize ions and generate stronger PRE resulting from the vortical plasma motions over the equator in the evening ionosphere (Lee et al., 2015) to supply additional plasma.

A combination of such effects as illustrated in Figure 5 leads to the extreme evening updrift of the F-layer during the solstice period under low solar-activity, ensuring suitable background conditions for the RT instability, where the strong initial seed perturbations by the volcano-induced disturbances could rapidly generate very intense EPBs. According to Tsunoda (2010a), neutral wind perturbations associated with circular gravity-waves are more efficient in generating a net field-line integrated polarization electric field, with the gravity-wave wavelength of the order or larger than the distance from the source. As the Lamb-wave propagation could continuously trigger concentric gravity-waves of wavelengths 500–1500 km (J. T. Lin et al., 2022), this would ensure sufficient polarization electric fields to provide seed perturbations. Thus, the unusually strong PRE and the ensuing sharp plasma density gradients, with the strong seed perturbations after the eruption resulted in rapid growth of the RT instability, yielding the super plasma bubbles.

The EPBs usually take about 1–2 hr to appear over low-latitude regions after onset. In the ROTI maps (Movie S1), over \sim 140°E, strong values expanding poleward appeared around 1010 UT over 31.3°N, with apex altitude of \sim 1660 km. The corresponding E-region sunset over equator was \sim 0917

UT, requiring the bubble \sim 53 min to reach such altitudes. Considering that EPBs are generated \sim 450 km, this suggests \sim 380 m/s vertical rise velocity for the bubbles. Over 145°E, the EPB rises with such large velocity, but is slower at 140°E (Figure S2 in Supporting Information S1). The estimated bubble rise velocities could be affected by the westward tilt and the eastward drift, and actual initial rise velocity could be even larger (Chou et al., 2021). Further, the TIDs that co-exist with the EPBs (Movie S1) could also contribute to the vertical rise velocity when the associated polarization electric fields are in phase with those within the bubbles. The strong westward tilt of EPBs point to such interactions (Chou et al., 2021).

These mechanisms operate most efficiently over the Asia-Pacific latitudes where the Lamb-wave over the equator almost coincides with E-region sunset (Figure 1; Movie S1), enabling intense PRE and super plasma bubbles. To less extent, similar processes favoring EPBs may extend across Indian and eastern African longitudes ($\sim 30^{\circ}$ E) where Lamb-wave progressively lags the terminator. No post-sunset irregularities occur over Africa where the

RAJESH ET AL. 7 of 10

19448007, 2022, 15, Downloaded from https://agupubs.onlinelibrary

wiley.com/doi/10.1029/2022GL099798, Wiley Online Library on [28/02/2023]. See the Terms and Conditions.

Acknowledgments

This work is partly supported by the

Ministry of Science and Technology

under MOST-110-2111-M-006-004

National Space Organization under

NSPO-S-110296. TM acknowledges

support from NSF awards AGS 1848544.

J. Yue and M. Y. Chou are supported by

NASA 80NSSC20K0628. The work is partly supported by NARL-NICT collab-

orative project. The authors acknowledge

the GNSS networks of GeoNet project

Geospatial Information Authority Japan,

Central Weather Bureau Taiwan, Hong

Kong Satellite Positioning Reference

Station Network, EUREF Permanent

GNSS Network and their data centers

Cartographic and Geological Institute

Ionospheric Network, Brazilian Institute

of Catalunya, Canadian High Arctic

of Geography and Statistics (IBGE),

National Seismological Center, Univer-

national Geodetic Network, International

GNSS Service (IGS), African Geodetic

Reference Frame (AFREF), TrigNet Web

South Africa, and British Isles continuous

GNSS Facility (BIGF) for GNSS data,

Bureau of Meteorology of Australia for

and Space Weather Services of the

ionograms.

sity of Chile, RESIF-RENAG French

New Zealand, Geoscience Australia.

and MOST-111-2119-M-006-001 and

difference exceeds a few hours (Figure S1 in Supporting Information S1), showing that Lamb-wave alone might not generate EPBs and should be timed with PRE.

5. Conclusion

Reduced E-region conductivity by the passage of Lamb-wave after the Tonga volcano eruption during sunset enables strong PRE in the solstice period, amplified by enhanced zonal winds and negative storm response over EIA. Under such conditions, rapidly up-drifting irregularities are generated with seed perturbations from the Lamb-wave driven gravity-waves, producing super plasma bubbles reaching extremely poleward latitudes. The results, for the first-time, show such intense EPBs by a volcanic eruption, highlighting the unprecedented space weather impacts triggered by a dramatic seismic event.

Data Availability Statement

The GNSS, GIS and IVM data are available at https://doi.org/10.6084/m9.figshare.19913590.v3. The ionograms are available at the Bureau of Meteorology, Government of Australia (https://www.sws.bom.gov.au/HF_Systems/1/3) and National Institute of Information and Communications Technology, Japan (https://wdc.nict.go.jp/ionog/js_viewer/js_01.html).

References

- Aa, E., Huang, W., Liu, S., Ridley, A., Zou, S., Shi, L., et al. (2018). Midlatitude plasma bubbles over China and adjacent areas during a magnetic storm on 8 September 2017. Space Weather, 16(3), 321–331. https://doi.org/10.1002/2017SW001776
- Aa, E., Zhang, S.-R., Erickson, P. J., Vierinen, J., Coster, A. J., & Goncharenko, L. P. (2022). Significant ionospheric hole and equatorial plasma bubbles after the 2022 Tonga volcano eruption (Vol. 20). Space Weather. e2022SW003101. https://doi.org/10.1029/2022SW003101
- Aarons, J. (1991). The role of the ring current in the generation or inhibition of equatorial F layer irregularities during magnetic storms. *Radio Science*, 26(4), 1131–1149. https://doi.org/10.1029/91RS00473
- Abdu, M. A., Alam Kherani, E., Batista, I. S., de Paula, E. R., Fritts, D. C., & Sobral, J. H. A. (2009). Gravity wave initiation of equatorial spread F/plasma bubble irregularities based on observational data from the SpreadFEx campaign. *Annals of Geophysics*, 27(7), 2607–2622. https://doi.org/10.5194/apages.27.2607.2009
- Abdu, M. A., Bittencourt, J. A., & Batista, I. S. (1981). Magnetic declination control of the equatorial F region dynamo electric field development and spread F. *Journal of Geophysical Research*, 86(A13), 11443–11446. https://doi.org/10.1029/JA086iA13p11443
- Berkner, L. V., & Wells, H. W. (1934). F-region ionosphere-investigations at low latitudes. *Terrestrial Magnetism and Atmospheric Electricity*, 39(3), 215–230. https://doi.org/10.1029/TE039i003p00215
- Burke, W. J., Gentile, L. C., Huang, C. Y., Valladares, C. E., & Su, S. Y. (2004). Longitudinal variability of equatorial plasma bubbles observed by DMSP and ROCSAT-1. *Journal of Geophysical Research*, 109(A12), A12301. https://doi.org/10.1029/2004JA010583
- Cherniak, I., & Zakharenkova, I. (2016). First observations of super plasma bubbles in Europe. Geophysical Research Letters, 43(21), 11137–11145. https://doi.org/10.1002/2016GL071421
- Chou, M.-Y., Lin, C. C. H., & Huba, J. D. (2021). Modeling the disappearance of equatorial plasma bubble by nighttime medium-scale traveling ionospheric disturbances. *Terrestrial, Atmospheric and Oceanic Sciences*, 32(2), 217–228. https://doi.org/10.3319/TAO.2021.03.30.01
- Chou, M.-Y., Pedatella, N. M., Wu, Q., Huba, J. D., Lin, C. C. H., Schreiner, W. S., et al. (2020). Observation and simulation of the development of equatorial plasma bubbles: Post-sunset rise or upwelling growth? *Journal of Geophysical Research: Space Physics*, 125(12), e2020JA028544. https://doi.org/10.1029/2020JA028544
- Dungey, J. W. (1956). Convective diffusion in the equatorial F region. *Journal of Atmospheric and Terrestrial Physics*, 9(5–6), 304–310. https://doi.org/10.1016/0021-9169(56)90148-9
- Farley, D. T., Balsey, B. B., Woodman, R. F., & McClure, J. P. (1970). Equatorial spread F: Implications of VHF radar observations. *Journal of Geophysical Research*, 75(34), 7199–7216. https://doi.org/10.1029/JA075i034p07199
- Fuller-Rowell, T. J., Codrescu, M. V., Rishbeth, H., Moffett, R. J., & Quegan, S. (1996). On the seasonal response of the thermosphere and ionosphere to geomagnetic storms. *Journal of Geophysical Research*, 101(A2), 2343–2353. https://doi.org/10.1029/95JA01614
- Glover, F. N. (1960). A survey of spread F. NBS Tech. Note (Vol. 82).
- Hanson, W. B., & Sanatani, S. (1973). Large Ni gradients below the equatorial F peak. *Journal of Geophysical Research*, 78(7), 1167–1173. https://doi.org/10.1029/JA078i007p01167
- Harding, B. J., Wu, Y.-J. J., Alken, P., Yamazaki, Y., Triplett, C. C., Immel, T. J., et al. (2022). Impacts of the January 2022 Tonga volcanic eruption on the ionospheric dynamo: ICON-MIGHTI and Swarm observations of extreme neutral winds and currents. Geophysical Research Letters, 49(9), e2022GL098577. https://doi.org/10.1029/2022GL098577
- Huang, C., & Hairston, M. R. (2015). The postsunset vertical plasma drift and its effects on the generation of equatorial plasma bubbles observed by the C/NOFS satellite. *Journal of Geophysical Research: Space Physics*, 120(3), 2263–2275. https://doi.org/10.1002/2014JA020735
- Huba, J. D., Drob, D. P., Wu, T.-W., & Makela, J. J. (2015). Modeling the ionospheric impact of tsunami-driven gravity waves with SAMI3: Conjugate effects. Geophysical Research Letters, 42(14), 5719–5726. https://doi.org/10.1002/2015GL064871
- Hysell, D. L. (2000). An overview and synthesis of plasma irregularities in equatorial spread F. Journal of Atmospheric and Terrestrial Physics, 62(12), 1037–1056. https://doi.org/10.1016/S1364-6826(00)00095-X
- Hysell, D. L., & Burcham, J. D. (1998). JULIA radar studies of equatorial spread F. Journal of Geophysical Research, 103(A12), 29155–29167. https://doi.org/10.1029/98JA02655
- Kelley, M. C., Larsen, M. F., LaHoz, C., & McClure, J. P. (1981). Gravity wave initiation of equatorial spread F: A case study. *Journal of Geophysical Research*, 86(A11), 9087–9100. https://doi.org/10.1029/JA086iA11p09087

RAJESH ET AL. 8 of 10

- Le, G., Liu, G., Yizengaw, E., & Englert, C. R. (2022). Intense equatorial electrojet and counter electrojet caused by the 15 January 2022, Earth and space science open archive. Retrieved from https://www.essoar.org/doi/abs/10.1002/essoar.10511040.2
- Lee, W. K., Kil, H., Kwak, Y.-S., & Paxton, L. J. (2015). Morphology of the postsunset vortex in the equatorial ionospheric plasma drift. Geophysical Research Letters, 42(1), 9–14. https://doi.org/10.1002/2014GL062019
- Lin, C. H., Liu, J. Y., Tsai, H. F., & Cheng, C. Z. (2007). Variations in the equatorial ionization anomaly peaks in the Western Pacific region during the geomagnetic storms of April 6 and July 15, 2000. Earth Planets and Space, 59(5), 401–405. https://doi.org/10.1186/bf03352701
- Lin, C.-Y., Lin, C. C.-H., Liu, J.-Y., Rajesh, P. K., Matsuo, T., Chou, M.-Y., et al. (2020). The early results and validation of FORMOSAT-7/COSMIC-2 space weather products: Global ionospheric specification and Ne-aided Abel electron density profile. *Journal of Geophysical Research: Space Physics*, 125(10), e2020JA028028. https://doi.org/10.1029/2020JA028028
- Lin, C. Y., Matsuo, T., Liu, J. Y., Lin, C. H., Huba, J. D., Tsai, H. F., & Chen, C. Y. (2017). Data assimilation of ground- based GPS and radio occultation total electron content for global ionospheric specification. *Journal of Geophysical Research: Space Physics*, 122(10), 10876–10886. https://doi.org/10.1002/2017JA024185
- Lin, J. T., Lin, C. H., Lin, C. Y., Pedatella, N. M., Rajesh, P. K., Matsuo, T., & Liu, J. Y. (2019). Revisiting the modulations of ionospheric solar and lunar migrating tides during the 2009 stratospheric sudden warming by using global ionosphere specification. Space Weather, 17(5), 767–777. https://doi.org/10.1029/2019SW002184
- Lin, J. T., Lin, C. H., Rajesh, P. K., Yue, J., Lin, C. Y., & Matsuo, T. (2020). Local-time and vertical characteristics of quasi-6-day oscillation in the ionosphere during the 2019 Antarctic sudden stratospheric warming. *Geophysical Research Letters*, 47(21), e2020GL090345. https://doi. org/10.1029/2020GL090345
- Lin, J.-T., Rajesh, P. K., Lin, C. C. H., Chou, M.-Y., Liu, J.-Y., Yue, J., et al. (2022). Rapid conjugate appearance of the giant ionospheric lamb wave signatures in the northern hemisphere after Hunga-Tonga volcano eruptions. *Geophysical Research Letters*, 49(8), e2022GL098222. https://doi.org/10.1029/2022GL098222
- Ma, G., & Maruyama, T. (2006). A super bubble detected by dense GPS network at East Asian longitudes. Geophysical Research Letters, 33(21), L21103. https://doi.org/10.1029/2006GL027512
- McClure, J. P., Singh, S., Bamgboye, D. K., Johnson, F. S., & Kil, H. (1998). Occurrence of equatorial F region irregularities: Evidence for trop-ospheric seeding. *Journal of Geophysical Research*, 103(A12), 29119–29135. https://doi.org/10.1029/98JA02749
- Mendillo, M., Baumgardner, J., Pi, X., Sultan, P. J., & Tsunoda, R. (1992). Onset conditions for equatorial spread F. Journal of Geophysical Research, 97(A9), 13865–13876. https://doi.org/10.1029/92JA00647
- Mendillo, M., Meriwether, J., & Biondi, M. (2001). Testing the thermospheric neutral wind suppression mechanism for day-to-day variability of equatorial spread F. *Journal of Geophysical Research*, 106(A3), 3655–3663. https://doi.org/10.1029/2000JA000148
- equatorial spread F. Journal of Geophysical Research, 106(A3), 3653–3663. https://doi.org/10.1029/2000JA000148

 Nishioka, M., Saito, A., & Tsugawa, T. (2008). Occurrence characteristics of plasma bubble derived from global ground-based GPS receiver
- networks. Journal of Geophysical Research, 113(A5), A05301. https://doi.org/10.1029/2007JA012605
 Ossakow, S. L. (1981). Spread-F theories-a review. Journal of Atmospheric and Terrestrial Physics, 43(5–6), 437–452. https://doi.
- org/10.1016/0021-9169(81)90107-0
 Pi, X., Mannucci, A. J., Lindqwister, U. J., & Ho, C. M. (1997). Monitoring of global ionospheric irregularities using the worldwide GPS network.
- Geophysical Research Letters, 24(18), 2283–2286. https://doi.org/10.1029/97GL02273
- Rajesh, P. K., Lin, C. H., Chen, C. H., Chen, W. H., Lin, J. T., Chou, M. Y., et al. (2017). Global equatorial plasma bubble growth rates using ionosphere data assimilation. *Journal of Geophysical Research: Space Physics*, 122(3), 3777–3787. https://doi.org/10.1002/2017JA023968
- Rajesh, P. K., Lin, C. H., Chen, C. H., Lin, J. T., Matsuo, T., Chou, M. Y., et al. (2017). Equatorial plasma bubble generation/inhibition during 2015 St. Patrick's Day storm. Space Weather, 15(9), 1141–1150. https://doi.org/10.1002/2017SW001641
- Rajesh, P. K., Lin, C. H., Lin, C. Y., Chen, C. H., Liu, J. Y., Matsuo, T., et al. (2021). Extreme positive ionosphere storm triggered by a minor magnetic storm in deep solar minimum revealed by FORMOSAT-7/COSMIC-2 and GNSS observations. *Journal of Geophysical Research: Space Physics*, 126(2), e2020JA028261. https://doi.org/10.1029/2020ja028261
- Rajesh, P. K., Lin, C. H., Lin, J. T., Lin, C. Y., Yue, J., Matsuo, T., et al. (2021). Day-to-day variability of ionosphere electron density during solar minimum derived from FORMOSAT-7/COSMIC-2 measurements. *Terrestrial, Atmospheric and Oceanic Sciences*, 32(6.1), 959–975. https://doi.org/10.3319/TAO.2021.08.01.01
- Rastogi, R. G., Mullen, J. P., & MacKenzie, E. (1981). Effect of geomagnetic activity on equatorial radio VHF scintillations and spread F. Journal of Geophysical Research, 86(A5), 3661–3664. https://doi.org/10.1029/JA086iA05p03661
- Richmond, A. D., & Fang, T.-W. (2015). Electrodynamics of the equatorial evening ionosphere: 2. Conductivity influences on convection, current, and electrodynamic energy flow. *Journal of Geophysical Research: Space Physics*, 120(3), 2133–2147. https://doi.org/10.1002/2014JA020935
- Richmond, A. D., Fang, T.-W., & Maute, A. (2015). Electrodynamics of the equatorial evening ionosphere: 1. Importance of winds in different regions. *Journal of Geophysical Research: Space Physics*, 120(3), 2118–2132. https://doi.org/10.1002/2014JA020934
- Sekar, R., & Kelley, M. C. (1998). On the combined effects of vertical shear and zonal electric field patterns on nonlinear equatorial spread F evolution. *Journal of Geophysical Research*, 103(A9), 20735–20747. https://doi.org/10.1029/98JA01561
- Shinagawa, H., Tsugawa, T., Matsumura, M., Iyemori, T., Saito, A., Maruyama, T., et al. (2013). Two-dimensional simulation of ionospheric variations in the vicinity of the epicenter of the Tohoku-Oki earthquake on 11 March 2011. *Geophysical Research Letters*, 40(19), 5009–5013. https://doi.org/10.1002/2013GL057627
- Sripathi, S., Banola, S., Emperumal, K., Suneel Kumar, B., & Radicella, S. M. (2018). The role of storm time electrodynamics in suppressing the equatorial plasma bubble development in the recovery phase of a geomagnetic storm. *Journal of Geophysical Research: Space Physics*, 123, 2336–2350. https://doi.org/10.1002/2017JA024956
- Sultan, P. J. (1996). Linear theory and modeling of the Rayleigh-Taylor instability leading to the occurrence of equatorial spread F. Journal of Geophysical Research, 101(A12), 26875–26891. https://doi.org/10.1029/96JA00682
- Sun, W., Kuriakose, A. K., Li, G., Yu, L., Zhao, X., Hu, L., et al. (2022). Unseasonal super ionospheric plasma bubble and scintillations seeded by the 2022 Tonga Volcano eruption related perturbations. *Journal of Space Weather Space Climate*, 12, 25. https://doi.org/10.1051/swsc/2022024
- Themens, D. R., Watson, C., Žagar, N., Vasylkevych, S., Elvidge, S., McCaffrey, A., et al. (2022). Global propagation of ionospheric disturbances associated with the 2022 Tonga volcanic eruption. *Geophysical Research Letters*, 49(7), e2022GL098158. https://doi.org/10.1029/2022GL098158
- Tsunoda, R. T. (2010a). On seeding equatorial spread F: Circular gravity waves. Geophysical Research Letters, 37(10), L10104. https://doi.org/10.1029/2010GL043422
- Tsunoda, R. T. (2010b). On seeding equatorial spread F during solstices. Geophysical Research Letters, 37(5), L05102. https://doi.org/10.1029/2010GL042576

RAJESH ET AL. 9 of 10

- Tsunoda, R. T., Bubenik, D. M., Thampi, S. V., & Yamamoto, M. (2010a). On large-scale wave structure and equatorial spread F without a post-sunset rise of the F layer. *Geophysical Research Letters*, 37(7), L07105. https://doi.org/10.1029/2009GL042357
- Valladares, C. E., Merriwether, J. W., Sheehan, R., & Biondi, M. A. (2002). Correlative study of neutral winds and scintillation drifts measured near the magnetic equator. *Journal of Geophysical Research*, 107(A7), 1112. https://doi.org/10.1029/2001JA000042
- Weber, E. J., Buchau, J., Eather, R. H., & Mende, S. B. (1978). North-south aligned equatorial airglow depletions. *Journal of Geophysical Research*, 83(A2), 712–716. https://doi.org/10.1029/JA083iA02p00712
- Whalen, J. A. (2002). Dependence of equatorial bubbles and bottomside spread F on season, magnetic activity, and E × B drift velocity during solar maximum. *Journal of Geophysical Research*, 107(A2), SIA31–SIA39. https://doi.org/10.1029/2001JA000039
- Whitney, H. E., & Malik, C. (1968). A proposed index for measuring ionospheric scintillation. Environmental Research Papers, (Vol. 284), Technical Report, Airforce Cambridge Research Laboratories. https://doi.org/10.21236/ad0669805
- Woodman, R. F., & La Hoz, C. (1976). Radar observations of F region equatorial irregularities. *Journal of Geophysical Research*, 81(31), 5447–5466. https://doi.org/10.1029/JA081i031p05447
- Wright, C., Hindley, N., Alexander, M. J., Barlow, M., Hoffmann, L., Mitchell, C., et al. (2022). Tonga eruption triggered waves propagating globally from surface to edge of space. *Earth and Space Science Open Archive*. https://doi.org/10.1002/essoar.10510674.1
- Wright, R. W., Koster, J. R., & Skinner, N. J. (1956). Spread F-layer echoes and radio-star scintillation. *Journal of Atmospheric and Terrestrial Physics*, 8(4–5), 240–246. https://doi.org/10.1016/0021-9169(56)90129-5
- Wu, T.-W., Huba, J. D., Krall, J., Fritts, D. C., & Laughman, B. (2015). Seeding equatorial spread F with turbulent gravity waves: Phasing effects. Geophysical Research Letters, 42(1), 15–21. https://doi.org/10.1002/2014GL062348
- Yokoyama, T. (2017). A review on the numerical simulation of equatorial plasma bubbles toward scintillation evaluation and forecasting. *Progress in Earth and Planetary Science*, 4(1), 37. https://doi.org/10.1186/s40645-017-0153-6
- Zettergren, M. D., Snively, J. B., Komjathy, A., & Verkhoglyadova, O. P. (2017). Nonlinear ionospheric responses to large-amplitude infrasonic-acoustic waves generated by undersea earthquakes. *Journal of Geophysical Research: Space Physics*, 122(2), 2272–2291. https://doi.org/10.1002/2016JA023159

RAJESH ET AL. 10 of 10